Calibrating micro-computed tomography data to permeability experiments and petrography – insights from Digital Rocks

By A. C. MONSEES, A. SUBHEDAR, B. BUSCH, B. NESTLER and C. HILGERS*

A. C. Monsees*, Dr. A. Subhedar**, Dr. B. Busch*, Prof. Dr. B. Nestler**, Prof. Dr. C. Hilgers*, *Structural Geology and Tectonics, Institute of Applied Geosciences, Karlsruhe Institute of Technology (KIT), **Institute for Digital Materials Science, Karlsruhe University of Applied Sciences & Institute of Applied Materials (KIT), E-mail:alexander.monsees@kit.edu

Abstract

Petrophysical measurements on core plugs integrated with petrographic information from thin-sections are established methods in reservoir quality assessment. X-ray micro-computed tomography (µCT) presents an opportunity to derive the internal structure of reservoir sandstones for digital fluid flow simulations, while simultaneously assessing mineral distribution in 3D based on mineral densities. We compare the single-phase permeabilities obtained with fluid flow simulations and experiments and discuss the anisotropic nature of the permeability tensor in both single- and two-phase flow. The results demonstrate a closer match for µCT porosity to petrophysical porosity compared to optical porosity, and an acceptable first order fit of the main mineralogical constituents. One-phase fluid flow simulations deliver results within 10–20 % of the laboratory measurements. Two-phase flow simulations enable the assessment of relative permeabilities in rocks with water-sensitive minerals. However, µCT-based fluid flow simulations are computationally very demanding and time consuming due to the heterogeneous nature of natural sandstone samples, and require a tradeoff between resolution, representative volume, and cost. Rock composition reconstructed from µCT images can be used as a first-order approximation for the composition of a sample, but is unable to confidently identify minerals that occur in minor quantities due to constraints of the chosen resolution. Thus, sandstone analyses by µCT cannot completely replace established methods.

Introduction

Petrographic analyses using thin-sections and petrophysical analyses utilizing core plugs are well established methods for reservoir characterization [1, 2]. “Digital Rocks” has become an established term, generally describing the digitization of structure and rock composition [3]. Computer tomography has been utilized at least over the last twenty years as an upscaling approach from 2D thin-sections to 3D petrography models, incorporating rock physics [3-5]. Advances in computational power over the last decade combined with the ongoing process of digitization present new opportunities regarding fluid flow simulations through porous siliciclastic sandstones [6-8].

We present digital rock volumes and numerical one- and two-phase fluid flow simulations based on x-ray micro-computed tomography (µCT) images. µCT is calibrated by petrophyiscal and petrographical laboratory analysis that determines porosity, permeability, and mineral distribution, highlighting the opportunities and challenges of digital rocks for petrophysical and mineralogical analysis (Fig. 1).

Materials and methods

Material and laboratory methods

A sample originating from the Upper Rotliegend siliciclastic Penrith Formation from the Vale of Eden half-graben (Cumbria, UK) is studied to highlight the approach. The particular sample was described in a petrographic study (sample BQ_1 in reference [9]). All petrophysical measurements are performed on a cylindrical sandstone plug (diameter: 25.4 mm, length: 40.0 mm) drilled parallel to bedding. The thin section taken from the plug cap compares to the x-z plane of the computed model detailed further below and outlines the rock composition on a grain scale. The normal to bedding is reflected by the y direction.

Petrophysical measurements include porosity and ambient permeability. Porosity was determined using helium pycnometry. Klinkenberg-corrected ambient permeability was measured at a constant confining pressure of 1.2 MPa with an air permeameter [10]. Permeability is the connected porosity and describes how easy a fluid can flow through porous media. It is commonly measured in millidarcy (mD).

The petrographic data is derived from a transparent thin-section prepared from the plug cap. The plug cap was impregnated with a blue-dyed epoxy resin to highlight porosity and prepared to a thickness of 30 µm. Point-counting (300 counts) was performed on a grid adjusted to the maximum grain size with a semi-automated Pelcon Point Counter installed on a Leitz Aristomet microscope. The error of point-counting is dependent on the amount of counts and the counts per category, and was statistically quantified within confidence levels of 95% [11].

The plug for micro-computed tomography (µCT) is drilled normal to the petrophysical plug axis after petrophysical measurements are completed. The µCT plug has a diameter of 6.5 mm and a length of 13.0 mm.

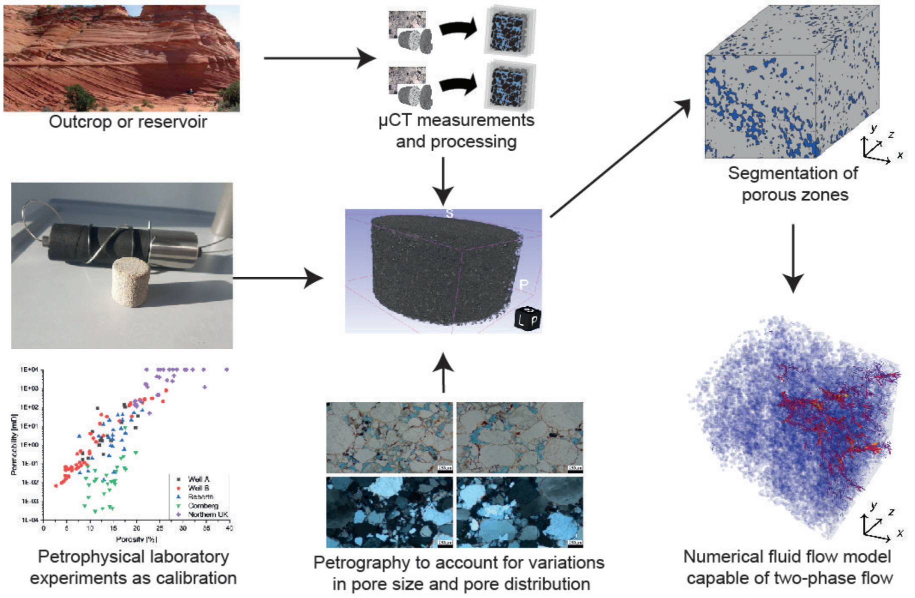

Fig. 1 Schematic overview of the workflow used to simulate two-phase flow in siliciclastic reservoir rocks

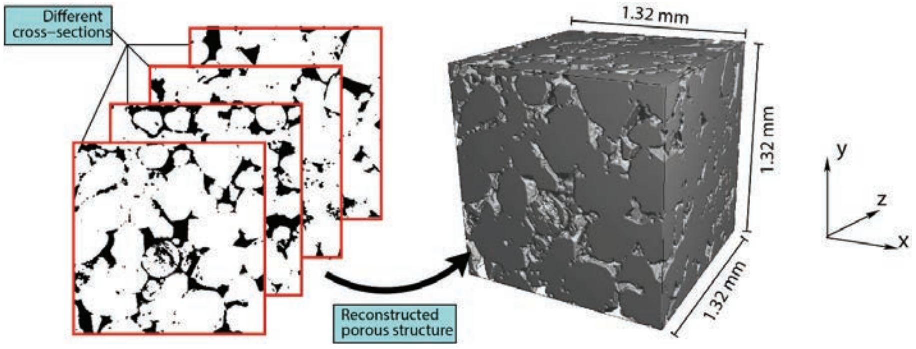

Fig. 2 Digitized 3D structure using the micro-CT images. This example demonstrates a 400 pixel block, with a resolution of 3.3 µm/px. Cross-sections on the left reflect the texture of the x-y plane at different positions in z direction

µCT methods

Micro-computed tomography (µCT) scans were performed by MITOS GmbH with an image resolution of 2048*2048 px. This results in a horizontal µCT resolution of 3.3 µm/px. Petrography and porosity measurements serve as calibration for the segmentation of pore-space in the µCT image batch. The permeability measurement on rock plugs is used as the benchmark for the results of single-phase fluid in digital rock flow simulations. Images from µCT were stacked and segmented with ImageJ, using helium porosity from rock plugs as a control factor on the segmented porosity (Fig. 2). Two image sequences are generated for µCT analysis: One for density-based mineralogy assessment, and one for fluid flow simulations. The mineralogy data set is exported as a gray-scale data set, while the simulation image sequence is exported as a binary color set, segmented for porosity and solids. Contrast enhancements are necessary in order to enable a more precise segmentation for porosity or mineralogy.

The Beer-Lambert law describes the interaction between an x-ray beam and the material [4]. The grayscale intensities are related to differences in x-ray attenuation of the respective minerals, which is parameter-specific and depends on atomic mass and density. It is incorporated in the Beer-Lambert law as attenuation coefficient [12]. For the mineral assessment, µCT images are imported in the CT processing program Slicer to render a high-resolution 3D petrographic model. The segmentation was conducted with the segmentation tool in Slicer, which is able to separate a 3D model into its constituents based on grayscale intensities. The grayscale color intensities are dependent on the attenuation of the respective minerals. Under consideration of the rock composition given by point-counting, grayscales in the stacked µCT images can be segmented for mineralogy based on grayscale thresholds. The total and relative volume of segmented classes can be checked or exported at any time, and is used as a quality check.

Simulation methods

For the purpose of solving fluid dynamical equations at the pore-scale, the color-gradient based lattice Boltzmann method is used in the present study. This method can deal with the wetting boundary condition and a range of fluid dynamic viscosity ratios. The numerical model's ability to capture these physical phenomena is tested with various benchmark tests. One of the main challenges of two-phase flow simulations lies in driving the flow through the narrow pores of digital rock structures. The numerical model utilizes a diffuse interface that can be as large as some of the pore throats, thus potentially unable to capture the capillary effects. As a compromise between the computational cost and reliability of simulations, numerical interface width is kept at six grid spacing. The simulation domain is a cube with dimensions of 1.32 mm (400*3.3 µm) in each direction (Fig. 2). The numerical interface width is then 6 times the grid spacing or roughly 19 micrometers. The cross-section images are in x and y direction for the fluid simulations (Fig. 2). These images are then stacked along z direction (Fig. 2).

For the evaluation of macroscopic properties (such as permeability) of generated digital structures, it is important to ensure that a sufficiently large domain is used. To choose such a volume, first, a series of single-phase permeability tests is carried out at increasingly large simulation domains. Once the permeability values obtained at two successive simulation domains are close to each other, this volume is chosen as the representative volume of the given sample. In this case, such a representative model is achieved with a cube of 400*400*400 pixel. This representative volume is then further utilized in the fluid flow simulations (Fig. 2).

One-phase flow

In the first step, single-phase intrinsic permeabilities of the sample are computed. For this purpose, a single-phase fluid is filled inside the simulation domain and is driven via gravity. The single-phase Darcy's law is

$$\bar{U} = \frac{K(-\nabla p + \rho g)}{\mu} \tag{1}$$

where $\bar{U}$ is the average fluid velocity, μ is dynamic viscosity, p is hydrodynamic pressure, g is the acceleration due to gravity, p is density and K is the intrinsic permeability tensor. The average fluid velocity is found as,

$$\bar{U} = \frac{1}{V}\sum U \tag{2}$$

where summation is carried out over entire volume V of the simulation domain and U is the local fluid velocity. The local fluid velocity U, in turn, is found from the solution of fluid dynamical equations via the lattice Boltzmann method. The density $\rho=1000$ kg/m^3 and dynamic viscosity $\mu=3\times10^{-4}$ Pa.s (water) is chosen for the single/-phase fluid in the simulations. The single-phase permeability of any porous medium depends upon its pore-geometry and – size alone, and is independent of the physical properties of the fluid used in the simulation. Thus, the simulated permeabilities can be compared directly with the experimental ones. To find the principal component of the permeability tensor K_{jj} (for brevity K_j is used hereafter), the component of the gravity vector g_j in the direction j is switched on. Direction j is a dummy variable running over the simulations in x, y and z direction successively. Periodic boundary condition is applied in the j direction while no-slip boundary condition is applied on the lateral sides. The bounce-back rule [13] is applied at the solid-fluid boundary to ensure the no–slip boundary condition.

Two-phase flow

The two-phase Darcy's law is

$$\bar{U}_i = k_i(S_w)\frac{K(-\nabla p + \rho_i g)}{\mu_i} \tag{3}$$

where the subscript i stands for the non-wetting gas (nw) or the wetting water (w) phase , k is the relative permeability and S_w is the saturation, which is the fraction of the wetting phase in the pore space. The average fluid velocity for the gas is computed as

$$\bar{U}_{nw} = \frac{1}{V}\sum U\frac{1-\varphi}{2}$$

$$\bar{U}_{w} = \frac{1}{V}\sum U\frac{1+\varphi}{2} \tag{4, 5}$$

where summation is carried out over entire volume V of the simulation domain, and φ is the local phase-field variable, which identifies gas and water phases. The phase-field variable takes values -1 and 1 in the bulk non-wetting gas phase and wetting water phase, respectively. Similar to the single-phase case, U and φ result from the numerical solution of fluid dynamical equations via the lattice Boltzmann method. The wetting (water) phase saturation is related to the phase-field variable as

$$S_w = \frac{1}{V}\sum\frac{1+\varphi}{2} \tag{6}$$

Capillary number Ca and viscosity ratio $M = \frac{\mu_w}{\mu_{nw}}$ are dimensionless numbers, which characterize the two-phase flow of the non-wetting fluid gas with the wetting fluid water on the pore-scale. The capillary number is defined as $Ca = \frac{\mu_{nw}U}{\sigma}$, where μ_{nw} is the viscosity of the non-wetting fluid gas, U is the characteristic fluid velocity and σ is the surface tension. The capillary number provides a relative dominance of viscous forces compared to the surface tension ones. In this work, the capillary number is approximately 10^{-4} indicating an interplay of viscous and capillary forces. The viscosity ratio M is chosen as 10 corresponding to the typical petroleum reservoirs. In addition, the wetting contact angle Θ is chosen as Θ =164°.

Laboratory results **Petrophysical results**	
Permeability 1040±30 mD (kx)	
Permeability	1040±30 mD (kx)
Helium porosity	18.0±0.3 %
Petrographic results	
Quartz	89.0±2.8 %
Feldspar	3.3±1.7 %
Optical Porosity	5.3±2.3 %
Iron oxides	0.0±0.4 %
Clay	2.3±1.3 %

Tab. 1 Experimental petrophysical and petrographic results with statistical error ranges.

Results

Laboratory results

The studied sample has a porosity of 18% and a Klinkenberg-corrected permeability of 1040 mD (1.026 $*10^{-9}$ m^2) (Tab 1). For the purpose of comparability with µCT data, petrographic results derived from point-counting (27 classes) have been simplified to five classes (Tab. 1). The sum of detrital and authigenic quartz, also including quartzite and mostly silicic rock fragments, is the most abundant constituent (89%). The second most abundant constituent is the optical porosity (5.3%), indicated by blue color in the thin-sections (Fig. 3), which comprises of intergranular and intragranular porosity. Feldspars (3.3%), including K-feldspars and plagioclases, are the third most abundant class. The remaining components were grouped into clays (2.3%), including mica as well as authigenic clay minerals, and iron oxides. Iron oxides occur in traces in the form of dust rims, and detrital grains and were not encountered during point-counting.

Digital rock results

Digital petrography and porosity

Mineral composition is derived from µCT images by enhancing contrast and comparing to the most abundant minerals in petrographic thin-section analysis (Fig. 4 a). The black color represents phases with the smallest density (porosity), while the highest densities are present as bright white areas. The major constituent (quartz) is dark gray (Fig. 4 a). The selected cube primarily consists of quartz (81.6%), and epoxy resin (porosity, 13.4%) (Tab. 2, Fig. 4 b). Minor constituents are clay minerals (2.1%), feldspars (1.6%) and iron oxides (1.3%) (Tab. 2, Fig. 4 b). The quantitative petrographic assessment by point-counting (Tab. 1) is used as a benchmark to threshold the µCT results (Tab. 2).

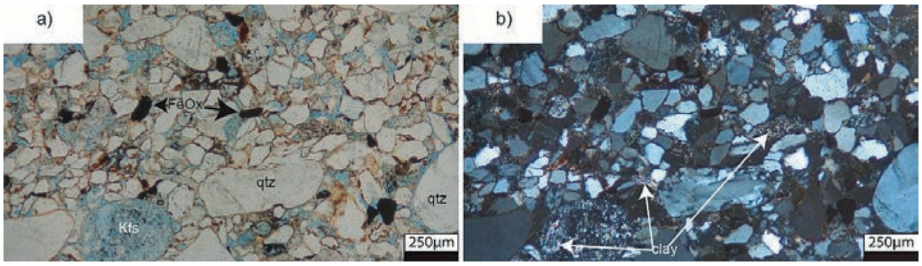

Fig. 3 Petrographic thin section of an exemplary reservoir rock analog from the plug cap of the studied sample. Porosity is colored with blue epoxy. a) The studied sample is dominated by detrital quartz and overgrown cements, which can be distinguished from the detrital quartz due to the brown-reddish hematite coats. Feldspar dissolution (kfs lower left) reflects the formation of secondary porosity during burial and uplift (further details about the diagenesis see reference [9]). Pictures in plane-polarized light. b) Arrows indicate small patches of clay minerals, mostly illite and mica, which occur as feldspar replacements or squeezed between the rigid grains. Picture in cross-polarized light. Qtz: quartz, Kfs: Potassium feldspar, FeOx: iron oxides.

Single phase fluid flow

The µCT image sequence intended for binary

Digital rock results	
Numerical results	
Permeability (one-phase flow)	1193 mD (k_x), 1585 mD (k_y), 827 mD (k_z)
Digital porosity	13.4%
Mineralogical results	
Quartz	81.6%
Feldspar	1.6%
Iron oxides	1.3%
Clay	2.1%
Clay	2.3±1.3%

Tab. 2 Results derived from µCT data for petrophysical simulation and petrographic data. Permeability was determined for all three principal directions

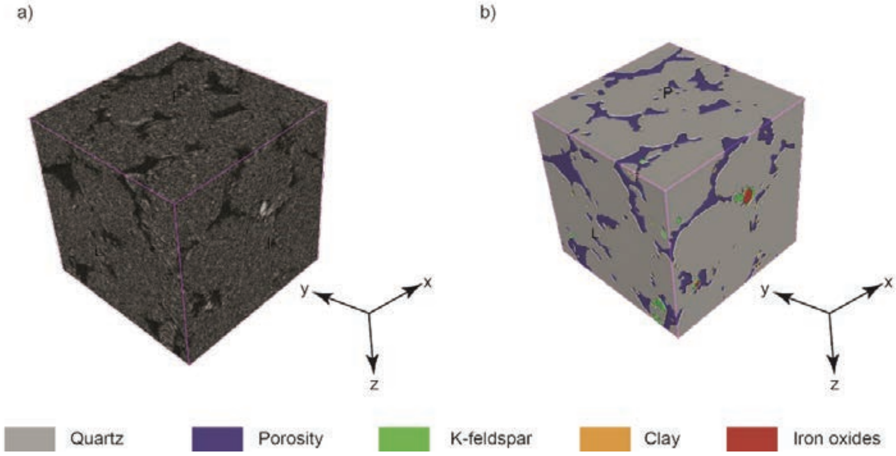

Fig. 4 a) Stacked µCT data after contrast enhancement and cropping into a cube with the dimensions of 400*400*400 px. Porosity in black, quartz, feldspar and clay in different shades of gray, and iron oxides as bright spots. b) Segmented µCT cube based on densities, coloring the distinguished classes porosity, quartz, feldspar, clay and iron oxides

image segmentation was divided into solid matter and minerals based on the porosity of 18% determined by helium pycnometry. Based on this porosity benchmark, a porous structure was generated in a 400*400*400 px cube. Under the influence of the applied gravity, the viscous forces continue to balance the effective pressure drop induced by the gravity until a steady-state is reached. The permeability of the porous medium is then computed via Eq. (1), where the average fluid velocity and the gravity induced pressure drop are known at the steady-state. This process is repeated for other principal directions to quantify the anisotropic nature of the permeability tensor. These principal components in the x, y and z directions turn out to be 1193 mD, 1585 mD and 827 mD, respectively (Tab. 2). Simulated permeabilities are slightly higher following bedding direction, and lowest in z direction. Zones of flow can be visualized as color-coded flow lines based on fluid velocity, highlighting the interconnected porosity of the sample (Fig. 5). Flowlines are calculated per direction (x, y, z) based on a pressure gradient. Therefore, it is only possible to display flowlines along one axis per figure.

Two phase flow

Initially, the mixture of two fluids, with a given fraction of the wetting fluid Sw, is distributed randomly inside the simulation domain. Similar to the single-phase case, gravity is used to drive the fluid flow in different principle directions [14, 15] with a no-slip boundary condition on the lateral directions. Due to the surface tension between the gas and water phases, the mixture slowly evolves to form distinguishable phases. Figure 6 shows the steady-state of the gas-water system at different water saturations when gravity is applied in the x direction. From these averaged fluid velocities and the known pressure drop created by the gravity, the relative permeabilities are evaluated and are shown in Figure 7. Relative permeability of one phase (e.g. gas) decreases, as the relative amount of another phase (e.g. water) increases. More gas (k_{nw}) will be produced until the water saturation in the rock reaches ~0.45 (x-direction), ~0.55 (y-direction), or 0.50 (z-direction). At higher water saturations, the permeability of water (k_w) is larger than of that

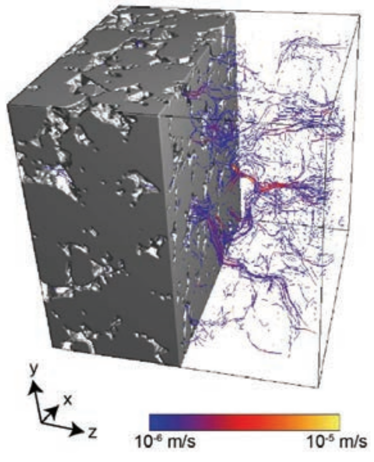

Fig. 5 Flow stream-lines of the local fluid velocity U, based on single-phase permeability simulation, here in z-direction. The color-coding represents the flow velocity and visualizes the interconnected flow-zones

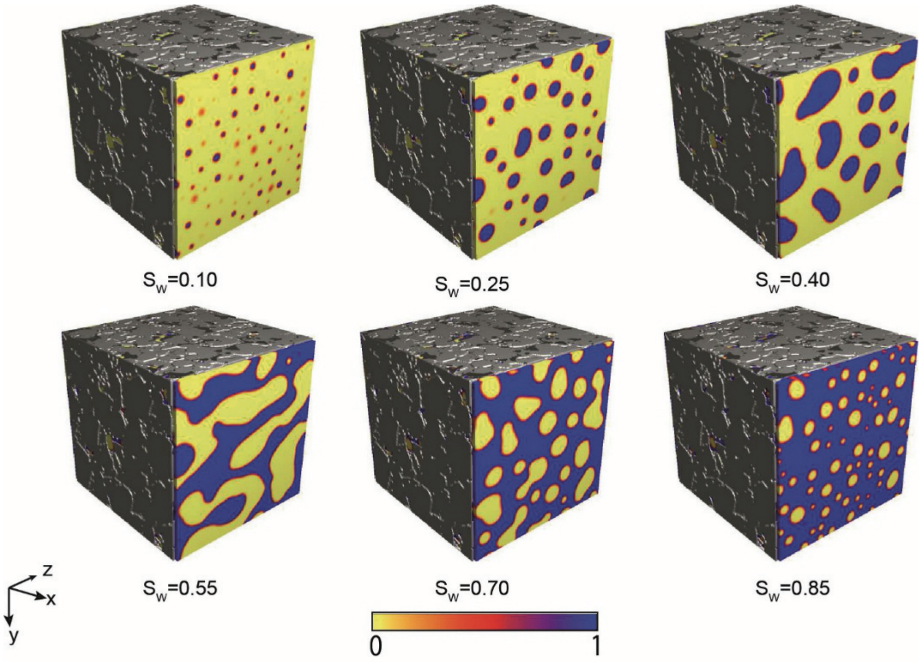

Fig. 6 Two-phase flow simulations at variable wetting-phase saturations. The blue color represents the wetting-phase (water) and the yellow color represents the non-wetting phase (gas). Steady-state configuration of gas-water flow under the action of gravity for different wetting saturation S_w

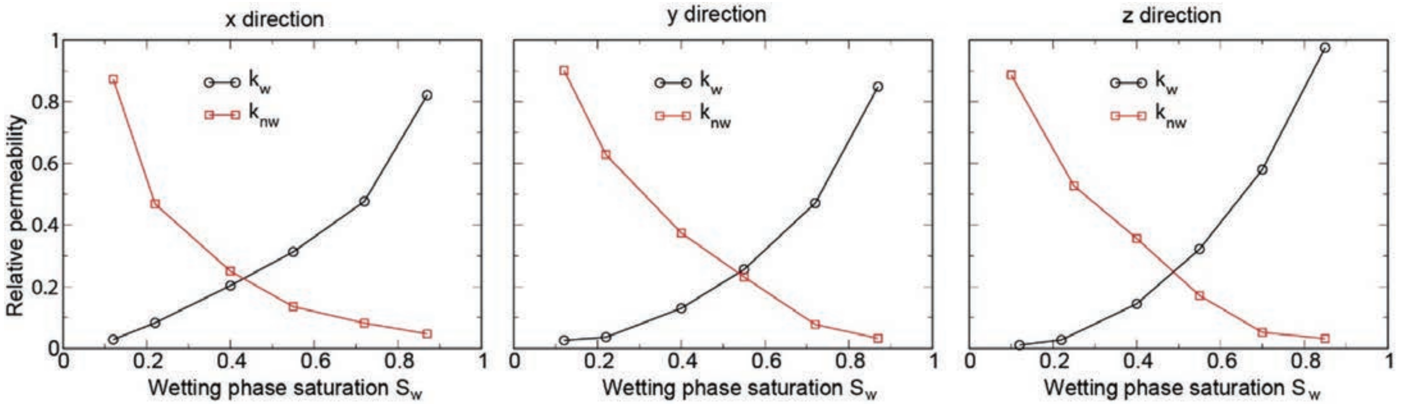

Fig. 7 Relative permeability curves in relation todependence of water saturation in the principal directions x, y and z. The water and gas are the wetting and non-wetting phases. The relative permeability is computed at certain intervals of water saturation to optimize computational time

gas (k_{nw}) and predominantly water will be produced (Fig. 7).

The relative permeability curves are determined for this sample from two-phase gas-water simulations (Fig. 7). For the evaluation of macroscopic properties (such as permeability) of generated digital structures, it is important to ensure that a sufficiently large domain is used. To choose such a volume, first, a series of single-phase permeability tests are carried out at increasingly large simulation domains. Once the permeability values obtained at two successive simulation domains are close to each other, this volume is chosen as the representative volume of the given sample. This representative volume is then further utilized in the two-phase simulations (Fig. 6). Two-phase simulations need to reach equilibrium in order to represent steady-state Darcy flow. The relative permeability under steady-state conditions is directly dependent on the saturation of the wetting phase (Fig. 6, 7).

Discussion

Rock composition

The conversion from 2D (thin-section) to 3D space (µCT digital rock) results causes a difference for the largest absolute mismatch of 7.4% in quartz content (laboratory: 89.0±2.8%, digital: 81.6%). Clay content (laboratory: 2.3±1.3%, digital: 2.1%) was confidently identified within the confidence levels, and is commonly reported as straight forward to identify [16]. Feldspars (laboratory: 3.3±1.7%, digital: 1.6%) match within their 95% confidence level error margins. Quartz and feldspar are minerals of very similar attenuation, leading to challenging segmentation [16]. This is interpreted as one reason for the match of digital and lab data for feldspars being barely within the confidence levels given by point-counting statistics. Another reason for the slight mismatch between digital and lab data is attributed to the partial dissolution of feldspars (Fig. 3 a), which results in segmentation of porosity instead of feldspar. The quality of the µCT segmentation for different rock minerals is also influenced by large attenuation contrasts of individual minerals like iron oxides. Compared to the predominant constituents like quartz, these result in large color contrasts (Fig. 4 a). The heaviest minerals (here: hematite/iron oxides) generate bright spots in the µCT images, which lead to uncertainty in the image segmentation (or binarization of image into porous space and solid structure) due to over-illumination of adjacent minerals. Due to the abundance obtained from point-counting (0±0.4%) compared with the abundance in the digital rock model (1.3%), an overestimation factor of three was assumed for high attenuation minerals.

Porosity

The optical porosity of 5.3% does not match with the petrophysical porosity of 18.0%. This general mismatch is well established and attributed to micro-porosity, sample heterogeneity and the fractal effects, leading to a general underestimation of porosity [17]. Porosity differences between laboratory results (18.0%) and digital rock results (13.4%) were observed. Considering the content of clay minerals, which are predominantly illite [9], microporosity in clays is able to partly explain the mismatch due to 63±10% microporosity in illites [18]. Due to 2.1% of clays in the digital rock model, this would amount to an additional 1.3±0.2%, resulting in a digital porosity of 14.7±0.2%.

Over-illumination effects due to large attenuation differences of iron oxides compared to quartz or porosity could also porosity lead to porosity being falsely segmented as iron oxides. However, it is not possible to exactly quantify the amount of porosity lost to that effect. At the very most, this may amount to 1%, which corresponds to the difference between digital and laboratory iron oxide abundance (Tab. 1, 2).

The µCT resolution of 3.3 µm introduces an additional uncertainty in segmentation, especially on grain boundaries, where very narrow open pore throats could either be segmented as porosity or as solid mineral. Further effects on digital porosity, which are hard to quantify, are microporosities in feldspars, which can reach up to 5% [19]. Assuming these microporosities in conjunction with 1.6% in digital feldspar abundance would result in the minor contribution <0.1% and thus not be a significant factor.

Considering all these effects, the digital porosity would be increased to roughly 15–16%. This is a closer representation of the petrophysical porosity. However, it needs to be considered that helium pycnometry can easily resolve porosity on a nanometer scale, while digital porosity is limited by resolution (here: 3.3µm). Similar offsets of 30–40 % between helium porosity and digital porosity without considering microporosity were also reported in other sandstone studies [20], confirming quality and validity of the results in this study.

Permeability

The simulated permeability in the x-direction of the sample corresponds well with the experimental measurements also performed along the x-direction of the sample. Although the porosity segmentation did mismatch by over 30%, permeability matches within in an acceptable range of ±10%. This is due to permeability being almost exclusively controlled by the large pores, which µCT is able to display easily. The bottleneck of microporosity in porosity segmentation is interpreted to not contribute to permeability. Therefore, µCT segmentation can be considered as effective porosity, explaining the good fit of digital permeability with laboratory permeability.

The spatial anisotropy of the studied sandstone, especially in relation to bedding, grain size, and rock composition, plays an important role in controlling the fluid behavior at the pore-scale and beyond. For instance, permeability values measured in simulations and experimental results are in agreement within 15% (k_x) (Tab. 1 & 2).

Close to water saturation (S_w=0.5), the relative permeability of the water phase is slightly higher than the gas phase in the x and z directions (Fig. 7). Given the higher wetting affinity of the water phase towards the solid porous medium, in fact, the opposite should be true. Thus, the simulations indicate that, in some cases, the initial random distribution of the gas-water phases may give rise to fluid patterns such that the gas phase is in contact with a larger surface area of the solid porous medium. According to the simulation, if water saturation exceeds 50% in two-phase flow normal to bedding, production of water starts.

An advantage of μCT simulations is the applicability in reservoir rocks consisting of water-sensitive minerals or water-sensitive cement phases like anhydrite, evaporites and carbonate cements. Two phase flow simulations could be used in these samples without altering the intrinsic permeability by dissolution of water-sensitive phases.

Conclusions

Our workflow links petrophysical rock and numerical digital rock permeability derived from μCT scans. Rock composition by μCT images and rock samples fall with in analysis bias.

The mismatch of higher petrophysical rock porosity is due to restricted resolution of μCT to segment for microporosity. This was observed to be less relevant for permeability simulations, as permeability is primarily controlled by large connected pores, which can easily be detected. Large attenuation contrasts result in over-illuminated bright spots, which lead to a systematic overestimation of the volume of very dense minerals (e.g. hematite) by a factor of three. Furthermore, highly porous fibrous clay minerals might easily be segmented as porosity, leading to an overestimation in both porosity and subsequent permeability simulations.

Fluid simulations present an opportunity to analyze and quantify the anisotropic nature of the permeability tensor, in both single- and two-phase flow. Differences between measured and simulated one-phase permeabilities are about 15% (experimental 1040 mD vs simulated 1190 mD). Results also highlight that the water production differs by almost 20% in the x-y-z direction of the simulated cube, and shows unexpected relative permeabilities. This suggests that water production starts at saturation levels where usually gas production is expected.

Overall, the tradeoff between resolution, representative volume and computational demands requires a case-by-case decision on how to process samples for μCT scans. Different shades of gray caused by molecular weight differences require pre-processing, mainly contrast enhancements, before mineral assessment based on grayscale intensity thresholds.

μCT-based mineralogy assessments can generally provide information about the major constituents, and μCT models can be used for fluid flow simulations easily highlighting permeability anisotropies for single and two-phase flow. However, it still requires the petrographic analysis since coats on mineral surfaces affecting wetting angles are not resolved by μCT.

Acknowledgements

The authors gratefully acknowledge research funding by the BMBF for the MERID project (Federal Ministry of Education and Research, research grants FKZ 03A0007A & FKZ 03G0868B). We thank MITOS GmbH for granting an academic discount on μCT analyses. D. Soyk and S. Kuchling (both DGMK) are thanked for project coordination. General impetus has been contributed by the programme "Renewable Energies", topic "Geothermal technologies (35.14.01)" of the Helmholtz association which is gratefully acknowledged.

References

[1] BUSCH, B.; HILGERS, C.; ADELMANN, D., Reservoir quality controls on Rotliegend fluvio-aeolian wells in Germany and the Netherlands, Southern Permian Basin – Impact of grain coatings and cements. Marine and Petroleum Geology, 2020. 112: p. 104075.

[2] MONSEES, A.C. et al., Rock typing of diagenetically induced heterogeneities – a case study from a deeply-buried clastic Rotliegend reservoir of the Northern German Basin. Marine and Petroleum Geology, 2020. 113: p. 104163.

[3] RASSENFOSS, S., Digital Rocks Out to Become a Core Technology. Journal of Petroleum Technology, 2011. 63: p. 36-41.

[4] VAN GEET, M.; SWENNEN, R.; WEVERS, M., Towards 3-D petrography: application of microfocus computer tomography in geological science. Computers & Geosciences, 2001. 27: p. 1091-1099.

[5] GOLAB, A.N. et al., 3D porosity and mineralogy characterization in tight gas sandstones. The Leading Edge, 2010. 29: p. 1476-1483.

[6] ANDRÄ, H. et al., Digital rock physics benchmarks—Part I: Imaging and segmentation. Computers & Geosciences, 2013. 50: p. 25-32.

[7] SAXENA, N. et al., References and benchmarks for pore-scale flow simulated using micro-CT images of porous media and digital rocks. Advances in Water Resources, 2017. 109: p. 211-235.

[8] PRAJAPATI, N. et al., Three-Dimensional Phase-Field Investigation of Pore Space Cementation and Permeability in Quartz Sandstone. JGR Solid Earth, 2018. 123: p. 6378-6396.

[9] BUSCH, B. et al., Cementation and structural diagenesis of fluvio-aeolian Rotliegend sandstones, northern England. Journal of the Geological Society, 2017. 174: p. 855-868.

[10] BECKER, I. et al., Porosity and permeability variations in a tight gas sandstone reservoir analogue, Westphalian D, Lower Saxony Basin, NW Germany: influence of depositional setting and diagenesis. Journal of Petroleum Geology, 2017. 40(4): p. 363-390.

[11] HOWARTH, R.J., Improved estimators of uncertainty in proportions, point-counting, and pass-fail test results. American Journal of Science, 1998. 298: p. 594-607.

[12] CURRY, T.S.; DOWDEY, J.E.; MURRY, R.C., Christensen's physics of diagnostic radiology. 1990, London: Lippincott Williams & Wilkins.

[13] ZOU, Q.; HE, X., On pressure and velocity boundary conditions for the lattice Boltzmann BGK model. Physics of Fluids, 1997. 9: p. 1591-1598.

[14] ZHAO, H. et al., Relative permeability of two immiscible fluids flowing through porous media determined by lattice Boltzmann method. International Communications in Heat and Mass Transfer, 2017. 85: p. 53-61.

[15] ZHAO, J. et al., The effect of wettability heterogeneity on relative permeability of two-phase flow in porous media: A lattice Boltzmann study. Water Resources Research, 2018. 54: p. 1295-1311.

[16] CNUDDE, V. et al., 3D characterization of sandstone by means of X-ray computed tomography. Geosphere, 2011. 7: p. 54-61.

[17] MARKUSSEN, Ø. et al., 3D characterization of porosity and authigenic cementation in Triassic conglomerates/arenites in the Edvard Grieg field using 3D micro-CT imaging. Marine and Petroleum Geology, 2019. 99: p. 265-281.

[18] HURST, A.; NADEAU, P.H., Clay Microporosity in Reservoir Sandstones: An Application of Quantitative Electron Microscopy in Petrophysical Evaluation. AAPG Bulletin, 1995. 79: p. 563-573.

[19] WALKER, F.D.L.; LEE, M.R.; PARSONS, I., Micropores and micropermeable texture in alkali feldspars: geochemical and geophysical implications. Mineralogical Magazine, 1995. 59: p. 505-534.

[20] PENG, S. et al., Using X-ray computed tomography in pore structure characterization for a Berea sandstone: Resolution effect. Journal of Hydrology, 2012. 472-473: p. 254-261.

Monsees, A. C.; Subhedar, A.; Busch, B.; Nestler, B.; Hilgers, C.
Calibrating micro-computed tomography data to permeability experiments and petrography – insights from Digital Rocks.
2020. Oil gas, (3/2020).
doi: 10.5445/IR/1000123827

Zitierung der Originalveröffentlichung:

Monsees, A. C.; Subhedar, A.; Busch, B.; Nestler, B.; Hilgers, C.
Calibrating micro-computed tomography data to permeability experiments and petrography – insights from Digital Rocks.
2020. Oil gas, (3/2020), 28–33.
doi:10.19225/200908